Accepted manuscript doi:
10.1680/jgeot.23.00263

Accepted manuscript doi:
10.1680/jgeot.23.00263

Submitted: 12 August 2023

Published online in 'accepted manuscript' format: 21 August 2024

Manuscript title: Approximate upper- and lower-bound analyses of translational rainfall-induced landslides in curvilinear hillslopes

Authors: Longfei Zhang[1], Wangcheng Zhang[2], Yang Wang[3], Ashraf Osman[2]

Affiliations: [1]Faculty of Earth Sciences and Engineering, Southwest Jiaotong University, Chengdu 611756, China,Formerly at Department of Engineering, Durham University, South Road, Durham, DH1 3LE, UK, [2]Department of Engineering, Durham University, South Road, Durham, DH1 3LE, UK, [3]Faculty of Engineering, China University of Geosciences, Wuhan 430074, China,

Corresponding author: Wangcheng Zhang Department of Engineering, Durham University, South Road, Durham, DH1 3LE, UK

E-mail: wangcheng.zhang@durham.ac.uk

Accepted manuscript doi:
10.1680/jgeot.23.00263

Abstract

Increased frequency of rainfall-induced landslides (RILs) with global climate change is expected to be a huge challenge. Previous studies have focused on RILs encompassing the examination of rotational failure mechanisms and straightforward slope geometries, notably those pertaining to planar or cutting slopes. However, instability issues of curvilinear hillslopes have received less attention, although they are of great significance for early warning landslides in more common natural slopes. This study presents a progressive failure mechanism for curvilinear hillslopes in which the local failure initiates at the steepest zone and gradually extends to upslope/downslope flat regions. By means of upper- and lower-bound analyses, approximate criteria for the onset of a translational landslide with respect to the critical wetting front depth and the failure positions are derived. Unlike traditional theories, upper- and lower-bound analyses are unaffected by slope topology, self-weight of soil, and cohesion effects. By conducting a case study at the end of the study, the suggested criteria exhibit notable merits in their straightforward implementation for evaluating the stability of curvilinear natural slopes under varying precipitation patterns.

Keywords: rainfall, progressive failure, shallow landslides, curvilinear slopes, limit analysis

Accepted manuscript doi:
10.1680/jgeot.23.00263

Introduction

Rainfall-induced landslides (RILs) cause huge economic losses and kill or injure untold numbers of people per year worldwide (Kjekstad & Highland 2009; Petley 2012). The frequency and severity of RILs have been significantly influenced by climate change through more intense heavy rainfalls (Gariano & Guzzetti 2016; Handwerger et al. 2019; Coe 2020). A striking example of this impact occurred in Tianshui, China, in 2013, where a substantial downpour triggered a total of 708 loess landslides, resulting in the loss of 24 lives and 2,386 houses (Wang et al. 2022). Similarly, on April 19, 2017, Manizales, Colombia, experienced 38 RILs, claiming 17 lives and affecting over 3,126 families (Correa et al. 2020). Nonetheless, prediction of RILs in terms of the landslide scale and triggering thresholds (e.g. rainfall intensity, and duration) remains a significant challenge in the field.

Often, RILs occur in residual soils on natural hillslopes (Zhu & Anderson 1998; Rahardjo et al. 2005), where the slip surface develops in a shallow depth (Dai et al. 2003; Zhang et al. 2011). In the past several decades, some hydro-mechanical models have been proposed to quantify RIL risks (Collins & Znidarcic 2004; Muntohar & Liao 2010; Conte & Troncone 2012; Zhan et al. 2013; Ran et al. 2018). One of them is the one-dimensional infinite slope model (ISM), in which the slope stability is performed by limit equilibrium methods (LEM) coupled with the hydrological response under rainfall infiltration (Iverson 2000; Casadei et al. 2003; Baum et al. 2008; Conte et al. 2022; Bianchi et al. 2022). However, ISM, which neglects the boundary effects, is only applicable to slopes with constant slope angle and the large length-to-thickness ratio of a developing landslide, as indicated by Griffiths et al. (2011) and Milledge et al. (2012).

Two- or three-dimensional approaches have also been developed (Burroughs 1985; Borga et

Accepted manuscript doi:
10.1680/jgeot.23.00263

al. 2002; Gabet & Dunne 2002; Vo & Russell 2017; Tran et al. 2018). Many of them employed the LEM, with a rotational failure mechanism, while translational landslides have been widely reported for shallow RILs (Gutierrez-Martin 2020). Besides, simplifications and assumptions have to be made in these models as well, e.g. ignoring the soil cohesion and/or the self-weight, adopting a horizontal ground surface above and below the slide, and restricting the slip surface to the soil-bedrock interface (Milledge et al. 2014). Most importantly, the mechanism associated with the rainfall infiltration and critical wetting front for the onset of a RIL in nonlinear slopes has been absent in most previous studies, which is of great interest for the early warning of RILs combined with rainfall data.

In the LEM, the stresses are assumed to be mobilised across the whole slip surface at the same instant, which can be the case for failure in planar or cutting slopes. However, for a RIL in curvilinear hillslopes, failure might be developed progressively from a local steep zone to flat regions (Lehmann & Or 2012) with upslope active failure and downslope passive failure (von Ruette et al. 2013; Cislaghi et al. 2019). In this case, the gentle upslope and downslope parts of a hillslope may help to stop the failure propagation, which has also been recognised in progressive submarine landslides (Puzrin et al. 2015; Puzrin 2016; Zhang et al. 2017, 2021). Nevertheless, the progressive failure mechanism during rainfall infiltration and its associated failure extensions for translational RILs are still open issues.

To close the aforementioned knowledge gaps, this study focuses on failure scale and critical wetting front depth for the onset of RILs in curvilinear hillslopes by using limit analysis. A novel failure mechanism of RILs is proposed considering progressive failure from the initiation and nucleation of the slip surface to the active/passive failure of sliding mass above the slip surface. Both approximate upper- and lower-bound criteria are proposed for determining the onset of slope instability, critical wetting front depth, and failure geometric scale, which are unaffected by slope

Accepted manuscript doi:
10.1680/jgeot.23.00263

topology, self-weight of soil, and cohesion effects.

1. MECHANISM OF RAINFALL-INDUCED TRANSLATIONAL LANDSLIDE

1.1. Rainfall infiltration and change in matric suction

Soils on hillslopes are usually unsaturated and strengthened by inter-pore matric suction. With a long period of drainage and evaporation, the profiles of moisture content and matric suction with respect to different water tables can be illustrated in Fig. 1a (Healy & Cook 2002). The capillary fringe serves as a transition zone connecting the lower saturated aquifer and the upper unsaturated zone, within which the soils are saturated or "quasi-saturated" due to capillary tension (Silliman et al. 2002). With a deep water table (see the solid line in Fig. 1a), the moisture content may reduce to its residual state from the ground surface to a certain depth with the suction maintained constant at the maximum when there is no tension crack, below which suction quickly decreases. With a shallow water table (see the dashed line in Fig. 1a), however, the residual state of moisture content may not be reached, and thus the matric suction decreases continuously along the soil depth. During rainfalls, rainwater percolation increases the moisture content of the soils, thereby reducing the suction, which may lead to hillslope instability. Before an eventual failure, soils may have undergone multiple wetting and drying cycles in history, leading to variations in the suction profile (Yates & Russell 2022).

Regardless of the water table depth, two different transient suction profiles may develop in homogeneous soils during rainfall infiltration: Type *a* (see green solid and dashed lines in Fig. 1b) is typically observed in fine-grained soils, where the suction is zero at the ground surface and gradually increases with soil depth, ultimately reaching its initial value at the wetting front (Lee et al. 2009); Type *b* with a distinct wetting front (see the red solid and dashed lines in Fig. 1b), where the soils behind the wetting front are saturated or nearly saturated, is common in coarse-grained soils (Zhang et al. 2018). The latter type is focused in this study considering intense

rainfalls in coarse-grained soils. The principles of unsaturated soil mechanics above the wetting front, applicable to certain fine-grained soils, will not be discussed further.

The assumption of a fully saturated zone behind the wetting front is anticipated to remain valid for at least two types of rainfall scenarios in coarse-grained soils: heavy rainfall events and continuous rainfalls during the rainy season. Ng et al. (2003) showed, through experimental tests, that daily rainfall of 60mm can induce a sudden suction change from 60 kPa to zero in a shallow depth. This suction change pattern has also been observed in field monitoring during rainy seasons, as reported by Jotisankasa and Mairaing (2010), where 20mm/day rainfall led to a loss of suction within a week. It's worth noting that the alteration in suction depends on both rainfall intensity and soil conditions, and in many instances, a gradual change may be observed (Yates and Russell, 2022).

Herein, the depth of the wetting front is denoted as h_w,and with a one-dimensional infiltration model, it can be determined based on Darcy's law and mass conservation (Green & Ampt 1911; Mein & Larson 1973). Within a long rainfall duration, the wetting front is independent of the slope angle (Cerdà & García-Fayos 1997; Chen & Young 2006), which is valid for a variety of residual soils, including the sandy loam, loam, silt loam, sandy clay loam, and clay loam (Chu-Agor et al. 2008; Jana et al. 2012).

Fig. 2 shows a schematic failure mechanism of RILs along the wetting front in a long curvilinear slope. Although the main findings are expected to not rely on the slope geometry, a set of exponential functions is used here for approximating the curvature of the hillslope and the slope-parallel wetting front (see Fig. 2). The wetting front can be expressed as

$$Z = \begin{cases} -H\left[1 - \exp\left(\frac{X}{H}\tan\beta_c\right)\right] & X < 0 \\ H\left[1 - \exp\left(-\frac{X}{H}\tan\beta_c\right)\right] & X \geq 0 \end{cases} \quad (1)$$

Accepted manuscript doi:
10.1680/jgeot.23.00263

where H is the half height of the slope, and β_c the maximum slope angle is located at the slope centre (see Fig. 2). The origin of the $X-Z$ coordinate system is set at the wetting front centre, and the ground surface can then be expressed as $Z_{GS} = Z + h_w$. By adjusting the values of H and β_c, the exponential function can generally fit most actual curvilinear hillslopes (Puzrin et al. 2015; Zhang et al. 2017).

1.2. Failure mechanism of RILs

A curvilinear hillslope can be divided into a set of small planar slope segments of the same length and different orientations. Prior to rainfall infiltration, matric suction aids in stabilizing the slope, and the safety factor for each slope segment can be calculated based on Coulomb's criterion (Fredlund & Rahardjo 1993)

$$F_s = \frac{\tan\varphi'}{\tan\beta} + \frac{c'}{\gamma h \cos\beta \sin\beta} + \frac{(\mu_a - \mu_w)\tan\varphi^b}{\gamma h \cos\beta \sin\beta} \quad (2)$$

where β is the slope angle; c' the effective cohesion; φ' the effective friction angle; γ the natural unit weight of the soil; h the depth of this point below the ground surface; μ_a the pore-air pressure, μ_w the pore-water pressure, $\mu_a - \mu_w$ the matric suction; and $\tan\varphi^b$ the change in shear strength per unit matric suction. During rainfalls, the matric suction in Eq. (2) disappears within the saturated soils above the wetting front, and hence the wetting front serves as the slip surface. The safety factor for each segment can be formulated as

$$F_s = \frac{\tan\varphi'}{\tan\beta} + \frac{c'}{\gamma_{sat} h_w \cos\beta \sin\beta} \quad (3)$$

where the γ_{sat} is the saturated unit weight of the soil.

A shallow translational failure mechanism is proposed for RILs as shown in the schematic Fig. 2, and its failure process is described as follows.

I. The local failure is initiated at the steepest point of a slope.

Accepted manuscript doi:
10.1680/jgeot.23.00263

II. With the continuing advancement of the wetting front, the failure is extended uphill and downhill progressively. Once the critical wetting front depth is reached, active failure occurs in the upslope area and results in tensile cracks at the ground surface.

III. The downslope passive failure may follow, at the same wetting front, immediately after the active failure, or later at a deeper wetting front.

2. LIMIT ANALYSIS SOLUTIONS

2.1. Assumptions and approximations

The main assumptions and approximations made for the limit analysis of RILs are outlined as follows.

I. The slope surface is symmetric with respect to the centre.

II. The slip surface is in alignment with the wetting front, which is parallel to the slope surface and higher than the groundwater table.

III. The infiltration behind the wetting front is a quasi-static process such that the net drag force applied on the soil skeleton essentially equals the gravitational force of inter-pore water.

IV. For the upper-bound analysis, the upslope active and downslope passive failure points have the same distance to the slope centre. This assumption is not adopted for the lower-bound analysis where the at-rest earth pressure influences the active/passive failure positions.

V. The soils satisfy Coulomb's failure criterion with an associated flow rule.

2.2. Approximate upper-bound analysis

The critical wetting front for RILs is of practical interest, as it is associated with the precipitation of a particular rainfall event and also provides the locus of the slip surface. To optimise the wetting front depth, a kinematically admissible failure mechanism is postulated, as

Accepted manuscript doi:
10.1680/jgeot.23.00263

shown in Fig. 3a, based on the upper-bound theorem. The failing slope can be divided into three parts, including a middle translational part BDEF, and two rotational parts ABD and EFG in upslope and downslope areas, respectively. The two rotational parts are assumed rigid and can geometrically be combined into a single log-spiral part ABGD, as shown in Fig. 3b. The kinematically admissible condition at boundaries of the three parts is guaranteed by assuming that points *D* and *E* are symmetric with respect to the centre, and the log-spirals AD and EG are tangent to the wetting front. The middle part is divided into a series of blocks with boundaries parallel to the chord r_0. The velocity and slope angle of each block can be represented by those on the intersection point between its right side and the basal slip surface, which becomes true when the length of the block is infinitely small. Velocities of the blocks are illustrated in the hodograph in Fig. 3c, where V_0, V_1, and V_k represent the velocities of blocks along the basal failure surface; $V_{1,0}$, $V_{2,1}$, and $V_{k,k-1}$ denote the relative velocities at the interface of two neighbouring blocks (see Fig. 3a). Especially, V_0, the velocity of the first block at point *D*, is $V_0 = \dot{\omega} r_0$ ($\dot{\omega}$ is the angular velocity of the rotational parts), to make it compatible with the rotational parts. Therefore, the velocity V_k of a block and the interfacial velocity $V_{k,k-1}$ can be calculated, according to trigonometric relations, as

$$V_k = \frac{V_0 \cos\varphi'}{\cos(\beta_k - \beta_0 + \varphi')}, V_{k,k-1} = V_k \frac{\sin(\beta_k - \beta_{k-1})}{\cos(\beta_{k-1} - \beta_0 + \varphi')} \tag{4}$$

where β_0 is the slope angle of the first block at point *D*, β_{k-1} and β_k the slope angles of blocks *k*-1 and *k*, respectively. The velocity vectors at key points are illustrated by arrows in Fig 3, which are inclined at an angle of φ' with respect to the velocity discontinuities, as the dilation angle is the same as the friction angle with an associated flow rule.

The log-spiral failure surface is expressed in a polar coordinate system with the origin at the rotation centre as

Accepted manuscript doi:
10.1680/jgeot.23.00263

$$r = r_0 \exp[(\theta - \theta_0)\tan\varphi'] \tag{5}$$

where r and θ are the polar coordinates; and r_0 and θ_0 are the polar coordinates at point *D*. According to Chen (1975) and Osman (2019), the exponent $\tan\varphi'$ can be derived from variational calculus and is valid for a Coulomb material with an associated flow rule. Assuming that the Cartesian coordinates of point *D* are (X_0, Z_0), coordinates at point *E* are then $(-X_0, -Z_0)$. From Eq. (1), X_0 and β_0 can be calculated based on Z_0. From the geometric relationship shown in Fig. 3a, the value of θ_0 is calculated as $\theta_0 = \pi/2 - \beta_0 + \varphi'$. Parameters controlling the assumed mechanism can be completely specified provided Z_0, r_0, and h_w are known, as indicated in Fig. 3a and listed in Table 1. Therefore, the critical wetting front depth h_w can be optimised based on the two variables r_0 and Z_0, as will be detailed later.

There are three types of energy involved in the proposed mechanism: gravitational potential energy, kinetic energy and friction dissipation. According to the first law of thermodynamics, the change in potential energy equals the energy dissipation, assuming the kinetic energy remains the same and minimal at the onset of failure, which is

$$\dot{W} = \dot{D} \rightarrow \bar{\dot{W}} = \bar{\dot{D}} \tag{6}$$

where $\dot{W}$ is the rate of work done by gravity (or change in potential energy) and $\dot{D}$ the energy dissipation rate, and $\bar{\dot{W}}$ and $\bar{\dot{D}}$ are the normalised $\dot{W}$ and $\dot{D}$ by $\dot{\omega}\gamma H^3$, respectively. With Eq. (4), the rate of work done by gravity (per unit width) in the middle part $\dot{W}^{\mathrm{mid}}$ can be formulated as

$$\begin{aligned} &\dot{W}^{\mathrm{mid}} = \lim_{n\to\infty} \sum_{k=1}^{n} \gamma V_k \sin(\beta_k - \varphi') A_k = 2\dot{\omega} r_0 \gamma h_w \cos\varphi' \int_0^{X_0} \frac{\sin(\beta - \varphi')}{\cos(\beta - \beta_0 + \varphi')} dX \\ &\rightarrow \bar{\dot{W}}^{\mathrm{mid}} = \frac{\dot{W}^{\mathrm{mid}}}{\dot{\omega}\gamma H^3} = \frac{h_w}{H} f_\gamma^{\mathrm{mid}} \end{aligned} \tag{7}$$

where A_k is the area of the block; $\bar{\dot{W}}^{\mathrm{mid}}$ is the normalised $\dot{W}^{\mathrm{mid}}$; and the parameter f_γ^{mid} is provided in Table 1. To calculate the rate of work done by gravity in the rotational parts ($\dot{W}^{\mathrm{rot}}$),

we assume a virtual soil block above the slope as shown by the shaded area in Fig. 3a. The rate of work can then be obtained by subtracting the work rate done by the virtual mass ($\dot{W}_{OABMG}$) from that done by the total mass ($\dot{W}_{OADG}$) as shown in Fig. 3b, that is

$$\dot{W}^{\mathrm{rot}} = \dot{W}_{OADG} - \dot{W}_{OABMG} \tag{8}$$

The value of $\dot{W}_{OADG}$ is given by (Chen 1975)

$$\dot{W}_{OADG} = \frac{1}{3}\dot{\omega} r_0^3 \gamma \int_{\theta_A}^{\theta_G} e^{3(\theta-\theta_0)\tan\varphi'} \cos\theta d\theta \rightarrow \bar{W}_{OADG} = \frac{\dot{W}_{OADG}}{\dot{\omega}\gamma H^3} = f_\gamma^{\mathrm{rot1}} \tag{9}$$

where respective θ_A and θ_G are the rotation angles of points *A* and *G*, as shown in Figs. 3a and 3b; parameter f_γ^{rot1} is provided in Table 1. The rate of work by the gravity of the virtual mass, $\dot{W}_{OABMG}$, is given by

$$\begin{aligned} &\dot{W}_{OABMG} = \gamma\dot{\omega}\left[\int_{X_{O_1}}^{X_A}\left(X - X_{O_1}\right)\left(Z_{AO_1} - Z_{GS}\right)dX + \int_{X_G}^{X_{O_2}}\left(X - X_{O_2}\right)\left(Z_{GO_2} - Z_{GS}\right)dX\right] \\ &\rightarrow \bar{W}_{OABMG} = \frac{\dot{W}_{OABMG}}{\dot{\omega}\gamma H^3} = f_\gamma^{\mathrm{rot2}} + \frac{h_w}{H} f_\gamma^{\mathrm{rot3}} \end{aligned} \tag{10}$$

where X_A, X_G, X_{O_1}, X_{O_2} are the *X* coordinates at points *A*, *G*, O_1, and O_2, respectively, Z_{AO_1} and Z_{GO_2} are functions of *X* describing lines AO_1 and GO_2, respectively (refer to the supplementary materials for more details). Parameters f_γ^{rot2} and f_γ^{rot3} are the functions of Z_0 and r_0, and listed in Table 1. Therefore, combining Eqs. (7)–(10), the normalised rate of work done by gravity is

$$\bar{W} = \bar{W}^{\mathrm{mid}} + \bar{W}^{\mathrm{rot}} = f_\gamma^{\mathrm{rot1}} - f_\gamma^{\mathrm{rot2}} + \frac{h_w}{H}\left(f_\gamma^{\mathrm{mid}} - f_\gamma^{\mathrm{rot3}}\right) \tag{11}$$

The energy dissipation of the system occurs along the basal slip surface as well as the interfaces between the blocks in the middle translational part. The dissipation rate along the rotational log-spiral slip surface $\dot{D}^{\mathrm{rot}}$ is

$$\begin{aligned}&\dot{D}^{\mathrm{rot}} = \int_{\theta_A}^{\theta_G} c'(\dot{\omega} r \cos\varphi') \frac{r d\theta}{\cos\varphi'} = \frac{c'\dot{\omega} r_0^2}{2\tan\varphi'}\left[e^{2(\theta_G-\theta_0)\tan\varphi'} - e^{2(\theta_A-\theta_0)\tan\varphi'}\right] \\ &\rightarrow \bar{\dot{D}}^{\mathrm{rot}} = \frac{\dot{D}^{\mathrm{rot}}}{\dot{\omega}\gamma H^3} = f_{c'}^{\mathrm{rot}}\end{aligned} \tag{12}$$

with parameter $f_{c'}^{\mathrm{rot}}$ provided in Table 1. Combined with Eq. (4), the dissipation rate along the middle segment of the slip surface $\dot{D}^{\mathrm{mid1}}$ is given by

$$\begin{aligned}&\dot{D}^{\mathrm{mid1}} = \lim_{n\to\infty}\sum_{k=1}^{n} c' V_k \cos\varphi' S_k = 2\dot{\omega} r_0 c' \cos^2\varphi' \int_0^{X_0} \frac{\sqrt{1+Z'^2}}{\cos(\beta-\beta_0+\varphi')} dX \\ &\rightarrow \bar{\dot{D}}^{\mathrm{mid1}} = \frac{\dot{D}^{\mathrm{mid1}}}{\dot{\omega}\gamma H^3} = f_{c'}^{\mathrm{mid1}}\end{aligned} \tag{13}$$

where S_k is the length of the basal slip surface of the block; $Z' = \tan\beta$ the slope gradient; and parameter $f_{c'}^{\mathrm{mid1}}$ is provided in Table 1. The dissipation rate $\dot{D}^{\mathrm{mid2}}$ within the middle blocks can be calculated by (see details in the supplementary materials)

$$\begin{aligned}&\dot{D}^{\mathrm{mid2}} = \lim_{n\to\infty}\sum_{k=1}^{n} c' V_{k,k-1} \cos\varphi' l_k = 2\dot{\omega} r_0 c' \cos\varphi' \, h_w \cos(\beta_0-\varphi') \frac{\sin(\beta_c-\beta_0)}{\cos(\beta_c-\beta_0+\varphi')} \\ &\rightarrow \bar{\dot{D}}^{\mathrm{mid2}} = \frac{\dot{D}^{\mathrm{mid2}}}{\dot{\omega}\gamma H^3} = \frac{h_w}{H} f_{c'}^{\mathrm{mid2}}\end{aligned} \tag{14}$$

where l_k is the length of the interface between the blocks, which is assumed constant among blocks and approximately expressed as $l_k = h_w \cos(\beta_0 - \varphi')$; parameter $f_{c'}^{\mathrm{mid2}}$ is provided in Table 1. The normalised rate of energy dissipation is therefore (from Eqs. (12)–(14))

$$\bar{\dot{D}} = \bar{\dot{D}}^{\mathrm{rot}} + \bar{\dot{D}}^{\mathrm{mid1}} + \bar{\dot{D}}^{\mathrm{mid2}} = f_{c'}^{\mathrm{rot}} + f_{c'}^{\mathrm{mid1}} + \frac{h_w}{H} f_{c'}^{\mathrm{mid2}} \tag{15}$$

Combing Eqs. (6), (11), and (15), the critical wetting front depth h_w can be finally formulated as

$$\frac{h_w}{H} = \frac{f_{c'}^{\mathrm{rot}} + f_{c'}^{\mathrm{mid1}} + f_{\gamma}^{\mathrm{rot2}} - f_{\gamma}^{\mathrm{rot1}}}{f_{\gamma}^{\mathrm{mid}} - f_{\gamma}^{\mathrm{rot3}} - f_{c'}^{\mathrm{mid2}}} \tag{16}$$

As listed in Table 1, all parameters in Eq. (16) involved can be fully determined according to the three independent variables h_w, Z_0, and r_0. Therefore, a minimum h_w in Eq. (16) can be

Accepted manuscript doi:
10.1680/jgeot.23.00263

optimised with Z_0 and r_0. The flowchart for the application of the approximate upper-bound solution is shown in Fig. 4. The critical wetting front and relevant geometry parameters of the slip surface are optimised using the Optimisation Toolbox in MATLAB in the study.

2.3. Approximate lower-bound analysis

As shown in Fig. 5, a local coordinate system *x*-*z* is introduced for the lower-bound analysis, with *x* and *z* axes parallel and perpendicular to the slope, respectively. The origin of the coordinate system is put at the slope surface.

It is not feasible to obtain the complete stress state in a curved slope through analytical means. The effective normal stress σ_z' and shear stress τ_{zx} acting on a point behind the wetting front are estimated based on infinite slope conditions, which are expressed by (Puzrin et al. 2015; Zhang et al. 2017)

$$\begin{aligned} \sigma_z' &= \gamma_{sat} h \cos^2 \beta \\ \tau_{zx} &= \tau_{xz} = \gamma_{sat} h \cos \beta \sin \beta \end{aligned} \tag{17}$$

The effective stress equals the total stress during the advancement of the wetting front, as the water pressure is assumed to be zero (or equal to atmospheric pressure). This result can be equally obtained by assuming that the inter-pore water is fully supported by the soil skeleton during a quasi-static infiltration process. While adequate for a lengthy natural slope featuring a gradual change in curvature, the simplification of the stress state suggests that the solution presented here is an approximate lower bound solution. From Eq. (17), the shear stress τ_{zx} can be reformulated as $\tau_{zx} = \sigma_z' \tan \beta$ and is limited to Coulomb's failure criterion. Once the shear stress in Eq. (17) exceeds the shear resistance, the slip surface initiates. The slip surface grows with the advancement of the wetting front and, with certain growth, active and passive failures occur at upslope and downslope areas, respectively. Fig. 6a illustrates the stress states in Mohr's circles for active and passive failures behind the wetting front at a point where the slope angle is not greater

Accepted manuscript doi:
10.1680/jgeot.23.00263

than the internal friction angle ($\beta \leq \varphi'$). With Coulomb's failure criterion, the following stress states at the onset of failure need to be satisfied (see the geometric relationship in Mohr's circles in Fig. 6a)

$$(\sigma'_m - \sigma'_z)^2 + \tau_{zx}^2 = (c' \cot \varphi' + \sigma'_m)^2 \sin^2 \varphi' \tag{18}$$

where σ'_m is the mean stress. Substituting $\tau_{zx} = \sigma'_z \tan \beta$ into Eq. (18), the mean stress σ'_m is obtained as

$$\sigma'_m = \frac{\left(\sigma'_z + \frac{c' \sin 2\varphi'}{2}\right) \pm \sqrt{\left(\sigma'_z + \frac{c' \sin 2\varphi'}{2}\right)^2 - \cos^2 \varphi' \left[\sigma_z'^2 (1 + \tan^2 \beta) - c'^2 \cos^2 \varphi'\right]}}{\cos^2 \varphi'} \tag{19}$$

where negative and positive signs are for the active and passive cases, respectively, as illustrated in Fig. 6a. The slope-parallel failure stresses at active ($\sigma_x'^{f+}$) and passive ($\sigma_x'^{f-}$) failure states can be calculated by $2\sigma'_m - \sigma'_z$, and they are

$$\begin{aligned} \sigma_x'^{f+} &= \frac{(2 - \cos^2 \varphi')\sigma'_z + c' \sin 2\varphi' - 2\sqrt{\left(\sigma'_z + \frac{c' \sin 2\varphi'}{2}\right)^2 - \cos^2 \varphi' \left[\sigma_z'^2 (1 + \tan^2 \beta) - c'^2 \cos^2 \varphi'\right]}}{\cos^2 \varphi'} \\ \sigma_x'^{f-} &= \frac{(2 - \cos^2 \varphi')\sigma'_z + c' \sin 2\varphi' + 2\sqrt{\left(\sigma'_z + \frac{c' \sin 2\varphi'}{2}\right)^2 - \cos^2 \varphi' \left[\sigma_z'^2 (1 + \tan^2 \beta) - c'^2 \cos^2 \varphi'\right]}}{\cos^2 \varphi'} \end{aligned} \tag{20}$$

While at the point where the slope angle is greater than the internal friction angle ($\beta > \varphi'$), its active and passive failure states can be illustrated by Fig. 6b. Before the stress state on the red line increases to the value at the point *R* (intersection of the red line and linear envelope), the slope-parallel failure stresses at active and passive failure states can be calculated with Eq. (20). However, when the stress state on the red line exceeds the value at the point *R* following the advancement of the wetting front, the at-rest shear stress is limited to Coulomb's criterion. Accordingly, the lope-parallel earth pressure can be calculated as

$$\sigma'_x = \sigma_x'^{f} = \frac{(2 - \cos^2 \varphi')\sigma'_z + c' \sin 2\varphi'}{\cos^2 \varphi'} \tag{21}$$

The slope-parallel force at the active failure state P_a in the upslope region can be obtained by integrating the slope-parallel stress from the surface to the wetting front along the *z* direction, that is

$$P_a = \int_0^{h_w \cos\beta} \sigma_x'^{f_+} dz \tag{22}$$

Similarly, the slope parallel force at the passive failure state P_p in the downslope can be expressed by

$$P_p = \int_0^{h_w \cos\beta} \sigma_x'^{f_-} dz \tag{23}$$

At the slope centre, the slope-parallel force remains the same as the at-rest value (see Fig. 5) which can be expressed as

$$P_g = \frac{1}{2} K_0 \gamma_{sat} h_w^2 \cos^2\beta \tag{24}$$

where K_0 is the at-rest earth pressure coefficient. According to Newton's second law, the slope-parallel force at a position along the slope can be given by

$$P = \frac{1}{2} K_0 \gamma_{sat} h_w^2 \cos^2\beta_c + \int_0^{X_\beta} (\tau_s - \tau_g)\sqrt{1 + Z'^2} dX \tag{25}$$

where $\tau_g = \gamma_{sat} h_w \cos\beta \sin\beta$ is the gravity shear stress along the wetting front, $\tau_s = \gamma_{sat} h_w \cos^2\beta \tan\varphi' + c'$ the shear resistance, and X_β the position where the slope angle is at a value of β. As the shear stress exceeds the shear resistance in the unstable zone, as shown in Fig. 5, the slope-parallel force *P* reduces in upslope regions ($X \geq 0$) and can reach a minimum value at a certain position. At any fixed position in upslope regions, once the slope-parallel force (Eq. (25)) reaches the active earth pressure, active failure occurs. The criterion for the initiation of active failure is

Accepted manuscript doi:
10.1680/jgeot.23.00263

$$P \le P_a \rightarrow \frac{1}{2}K_0\gamma_{sat}h_w^2\cos^2\beta_c + \int_0^{X_\beta}(\tau_s - \tau_g)\sqrt{1+Z'^2}dX \le \int_0^{h_w\cos\beta}\sigma_x'^{f_+}dZ \tag{26}$$

Similarly, in the downslope part ($X \le 0$) the criterion for passive failure is given by

$$P \ge P_p \rightarrow \frac{1}{2}K_0\gamma_{sat}h_w^2\cos^2\beta_c + \int_0^{X_\beta}(\tau_s - \tau_g)\sqrt{1+Z'^2}dX \ge \int_0^{h_w\cos\beta}\sigma_x'^{f_-}dZ \tag{27}$$

For cohesionless soils with $c' = 0$, the failure stresses $\sigma_x'^{f_+}$ and $\sigma_x'^{f_-}$, respectively, can be simplified as

$$\begin{aligned}\sigma_x'^{f_+} &= \gamma_{sat}h\cos^2\beta\frac{(2-\cos^2\varphi') - 2\sqrt{1-\cos^2\varphi'(1+\tan^2\beta)}}{\cos^2\varphi'}\\ \sigma_x'^{f_-} &= \gamma_{sat}h\cos^2\beta\frac{(2-\cos^2\varphi') + 2\sqrt{1-\cos^2\varphi'(1+\tan^2\beta)}}{\cos^2\varphi'}\end{aligned} \tag{28}$$

at a point where the slope angle satisfies $\beta \le \varphi'$, and

$$\sigma_x' = \sigma_x'^{f} = \gamma_{sat}h\cos^2\beta\frac{(2-\cos^2\varphi')}{\cos^2\varphi'} \tag{29}$$

at a point where the slope angle satisfies $\beta > \varphi'$. The criteria for the active and passive failures in cohesionless soils can be obtained by the substitution of Eqs. (28) or (29) into Eqs. (26) and (27).

Notably, after the onset of the active failure, cracks develop and the unbalanced force of the failing upslope part is transferred to the downslope region. The increased slope parallel force might exceed the maximum, and hence the passive failure is initiated. While the downward part may sustain the failing part through active failure upslope, passive failure may still occur with the continued advancement of the wetting front, as illustrated by Fig. 2. The detailed procedure for determining the critical wetting front depths and active/passive failure locations with the lower-bound analysis is illustrated in Fig. 4.

3. RESULTS AND DISCUSSIONS

The proposed upper-bound limit analysis (UBLA) and lower-bound limit analysis (LBLA)

solutions are compared against the numerical results from the commercial software OptumG2 based on the finite element limit analysis method (Krabbenhoft, 2019). In addition, solutions from the ISM (Rahardjo et al. 1995), and the simplified planar slope models (SPSM) (Huang et al. 2022) are compared and discussed. Both the saturated and unsaturated soil mechanics are considered in the numerical analysis. Therefore, for the base case, the unit weight and matric suction of saturated soils behind the wetting front are $\gamma_{sat} = 20\ \mathrm{kN/m^3}$ and $\mu_a - \mu_w = 0\ \mathrm{kPa}$, respectively, while those ahead of the wetting front are $\gamma = 18\ \mathrm{kN/m^3}$ and $\mu_a - \mu_w = 50\ \mathrm{kPa}$, respectively. The at-rest earth pressure coefficient is simply $K_0 = 1 - \sin\varphi'$ as suggested by Jacky (1944), and the friction angle related to matric suction is $\varphi^b = 18°$. The cohesion and friction angle of the soils are $c' = 10\ \mathrm{kPa}$ and $\varphi' = 25°$, respectively. Three cases with different slope geometries (described by Eq. (1)) are analysed, and the geometry parameters are listed in Table 2.

Fig. 7 shows the numerical results for Case 2 with the OptumG2 Finite element UBLA, where Fig. 7a represents the initial state before rainfall with an initial factor of safety (FOS) of 1.127 and Fig. 7b denotes the critical state after certain advancement of wetting front with FOS being unity. A deep and rotational failure mechanism is recognised at the initial state, while with the advancement of the wetting front, a shallow and translational failure mechanism becomes apparent. The latter echoes the mechanism proposed in the study as shown in Fig. 3a. The depths of the critical wetting front for all three cases are listed in Table 2. Good agreement can be found between the results of the proposed UBLA and the finite element UBLA, with the biggest difference being only 0.06 m in Case 3. As expected, the LBLA provides lower predictions of critical wetting front depth than the UBLAs. Also, the critical depths obtained from the LBLA proposed in the study are (up to 21.98%) smaller than those obtained in the finite element LBLA

analysis, indicating more conservative estimations.

A comparison of the landslide scale between the proposed method and finite element limit analysis is also conducted, with results shown in Table 2. In the study, the landslide scale is measured as the horizontal distance between the two failure limits at the slope surface, say points *A* and *G*, as shown in Fig. 3a, which is denoted as *L*. For UBLA, it can be calculated directly based on the obtained geometry parameters listed in Table 1. For LBLA, slip surfaces developed in the sliding layer are inclined at an angle of $\pi/4 + \varphi'/2$ and $\pi/4 - \varphi'/2$ with respect to the slope-parallel direction for passive and active failure states, respectively. Similar to the critical wetting front depth, the landslide scale obtained from the proposed UBLA is close to that from the finite element UBLA, while a smaller landslide is predicted with the proposed LBLA compared to the finite element LBLA.

To intuitively compare with the numerical results, the obtained failure extensions for Case 2 by the proposed LBLA and UBLA are also presented and compared in Fig. 7b. The proposed UBLA gives a less extended failure in the upslope region while more extended in the downslope region, compared with the finite element UBLA results. This may be due to the assumption of symmetric failure limits to the slope centre made in the proposed UBLA method. The LBLA solutions depend on the initial slope-parallel force P_g and hence the at-rest earth pressure coefficient (see Eq. (24)). Strictly speaking, for the saturated zone behind the wetting front, the slope-parallel force induced by the two phases (i.e. water and soil) should be calculated separately, with the earth pressure coefficient applied on the soil phase only. For simplicity, a total stress analysis method was adopted to consider the slope-parallel force, which is conservative compared with the two-phase calculation mentioned above.

The ISM method is widely used in practice considering an infinitely long planar slope, and the upper-bound solution based SPSM method, proposed by Huang et al. (2022), is well applied to

Accepted manuscript doi:
10.1680/jgeot.23.00263

a cut slope. Their applicability and accuracy in long curvilinear slopes are tested by a comparison with the proposed UBLA method. In order to make a comparison between the methods, a curvilinear slope is simplified as a planar slope, as shown in Fig. 8a. Three different slope angles are selected to reflect the original slope geometry, including the smallest slope angle $\beta_{\min}$, the largest slope angle $\beta_{\max}$ (slope centre angle), and the middle slope angle β_{mid} averaged between $\beta_{\max}$ and $\beta_{\min}$. The smallest slope angle is determined as the inclination of the slope segment from the slope centre to the failure limit (point *A*, as shown in Fig. 3a).

The results are compared in Fig. 8b. It can be seen that except for the selected minimum slope angle in Cases 1 and 2 (compared with the proposed LBLA), the ISM produces the lowest estimation of the critical wetting front depth for all cases. The SPSM provides higher estimates of critical wetting front depth than the ISM. The results predicted by SPSM are smaller than those by the proposed UBLA if the maximum and middle slope angles are used. However, the SPSM gives a larger critical wetting front depth than the proposed UBLA if the smallest slope angle is used. This indicates that the selection of a representative slope angle in curvilinear hillslopes is important for an accurate slope stability analysis. Note that, in addition to predicting the critical wetting front depth, the proposed method in the study is also able to estimate the failure scale of curvilinear slopes, which is not easily achieved using the traditional ISM.

In order to investigate the influence of soil properties (c' and K_0) and slope geometry (β_c) on the critical wetting front depth and slide length (i.e. failure extension), a parametric study was conducted using the proposed methods. Reference parameters were adopted as: $\gamma_{sat} = 20$ kN/ m^3, $H = 50$ m, and $\varphi' = 25°$.

Fig. 9a illustrates the impact of cohesion on both the critical wetting front depth and slide length. The results indicate that as the cohesion of the soil increases, both the wetting front depth

Accepted manuscript doi:
10.1680/jgeot.23.00263

and slide length also increase. The LBLA method provides more conservative predictions compared to the proposed UBLA method. However, as the cohesion approaches zero, the differences between the results obtained from the proposed LBLA and UBLA become negligible. Fig. 9b presents the influence of the at-rest earth pressure coefficient (K_0) on the critical wetting front depth and failure scale. When using the LBLA method, an increase in K_0 results in a small increase in slide length, and leads to a slight reduction in the critical wetting front depth. Conversely, the UBLA method yields constant values for both the critical wetting front depth and slide length, regardless of variations in K_0.

As depicted in Fig. 9c, a decrease in the central slope angle leads to a rapid increase in the critical wetting front depth. A slope failure triggered solely by rainfall becomes unlikely when the angle is lower than 36°, as the critical wetting front exceeds the reach even during intense rainfall events. The slide length obtained from the UBLA method increases with decreasing β_c, while it slightly decreases using the proposed LBLA method when β_c is lower than 45°.

4. WORKED EXAMPLE

The proposed method is illustrated in this section, with an application in stability analysis of slopes during or after rainfalls in Peninsula, Malaysia. The soil properties were determined based on Lee et al. (2009) and listed in Table 3, where the at-rest earth pressure ratio K_0 is simply estimated as $1 - \sin\varphi' = 0.469$. According to RILs record in Genting Highlands resort area (see study area in Fig. 10a), the slope angle for RILs is usually between 35° to 45° (Tan & Ting 2008). Therefore, different hillslopes with constant $H = 300$ m and varied β_c were analysed using the proposed method. The matric suction profiles under different rainfall intensities and duration based on a ten-year return period are shown Fig. 10b, which was obtained by the Seep/W, and one can refer to Lee et al. (2009) for more details.

Accepted manuscript doi:
10.1680/jgeot.23.00263

A distinct wetting front can be observed in Fig. 10b, where the matric suction quickly changes from a very low value (close to zero) to a maximum value (initial matric suction before rainfalls). It is conservative to assume that the matric suction behind the wetting front all disappears. Therefore, the saturated unit weight was used for the soil behind the wetting front, which is 19.13 kN/m^3. Fig. 10c shows the critical wetting front against different slope angles at the slope centre.

The critical wetting front depth increases as the centre slope angle decreases in both UBLA and LBLA analyses. For a maximum slope angle of 46°, a 5-day or longer rainfall event can trigger a landslide, while for a maximum slope angle of 40°, only a 30-day rainfall event can trigger a failure. A slope failure is unlikely to happen for all considered rainfall events when the centre slope angle is below 38°. The wetting front reaches infinitely deep when the centre slope angle approaches 36°, which means no failure occurs at this angle as it is close to the friction angle of soils.

5. CONCLUSIONS

This study proposes a progressive failure mechanism of rainfall-induced shallow translational landslides in curvilinear hillslopes and criteria for critical wetting front and failure extension accordingly. The failure is considered to be initiated at the steepest region with its progressive growth into the upslope and downslope flat regions with rainfall infiltration. The approximate criteria for critical wetting front depth and failure extension were made based on the upper- and lower-bound limit analyses. The main conclusions are as follows.

(a) During rainfall infiltration, with the increase of moisture content, the matric suction in the soil decreases while the unit weight of the soil increases. Both changes contribute to the instability of a slope with the growth of an unstable zone and reduction in the soil mantle resistance. The slip surface develops gradually along the moving wetting front

until active/passive failures are achieved in the sliding layer above the slip surface.

(b) In the approximate lower-bound analysis considering force equilibrium, the active failure may occur first with the development of cracks. Passive failure occurs later with the release of failed soils. This is consistent with field observations, that is, under a rainfall event, a slope may only undergo active failure with the formation of upslope tensile cracks instead of global failure, which, however, can evolve into passive failure with continuing rainfalls and a deeper wetting front.

(c) In comparison with the finite element limit analysis, the proposed UBLA agrees well with it in critical wetting front depth, while the proposed UBLA gives a more conservative estimation; the failure extension would be slightly underestimated in the upslope region and be overestimated in the downslope region by the proposed UBLA, and the proposed LBLA provides a smaller failure region.

(d) The proposed method is applicable to a wide range of natural slopes, which considers the boundary effects of the curvilinear slope geometry that is absent in ISM and avoids the uncertainty of slope angle selection in SPSM. The wetting front depth and failure scale exhibit a positive correlation with soil cohesion. Furthermore, the LBLA findings indicate that an elevated at-rest earth pressure coefficient increases the failure scale and decreases the critical wetting front of a RIL, slightly.

ACKNOWLEDGEMENTS

The first author wants to acknowledge the China Scholarship Council (CSC) for support as a joint PhD scheme at Durham University under Grant No. 202206410030. The third author thanks the support from the National Natural Science Foundation of China (No. 42077277).

Accepted manuscript doi:
10.1680/jgeot.23.00263

Notations

H	half the height of the slope
β, β_c	slope angle and maximum slope angle at the slope centre, respectively
Z_{GS}	expression of the ground surface in the global coordinate system
Z'	slope gradient expressed as $Z' = \tan\beta$
h_w, h	depths of the wetting front and of an arbitrary point below the ground surface, respectively
c', φ'	effective cohesion and friction angle of the soil, respectively
γ, γ_{sat}	natural and saturated unit weights of the soil, respectively
μ_a, μ_w	pore-air and pore-water pressures, respectively
$\tan\varphi^b$	change in shear strength per unit matric suction
r, θ	polar coordinates
$r_0, \theta_0, r_A, \theta_A, r_G, \theta_G$	characteristic polar coordinates at key points
$Z_0, X_0, X_A, X_G, X_{O_1}, X_{O_2}$	characteristic Cartesian coordinates at key points
Z_{AO_1}, Z_{GO_2}	expressions of lines AO_1 and GO_2 in Fig. 3a, respectively.
$\Theta, \Theta_r, \Theta_s$	volumetric water content of the soil with the subscripts 'r' and 's' denoting saturated and residual situations, respectively.
S_r	residual matric suction in the soil corresponds to Θ_r
$\dot{W}, \dot{D}$	rate of work done by gravity and energy dissipation rate, respectively
$\bar{\dot{W}}, \bar{\dot{D}}$	normalised $\dot{W}$ and $\dot{D}$ by $\dot{\omega}\gamma H^3$, respectively
$\dot{W}^{\mathrm{mid}}, \bar{\dot{W}}^{\mathrm{mid}}$	$\dot{W}$ and normalised $\dot{W}$ of the middle part (BDEF) in Fig. 3a
$\dot{D}^{\mathrm{mid1}}, \bar{\dot{D}}^{\mathrm{mid1}}$	$\dot{D}$ and normalised $\dot{D}$ along the wetting front beneath the middle part in Fig. 3a
$\dot{D}^{\mathrm{mid2}}, \bar{\dot{D}}^{\mathrm{mid2}}$	$\dot{D}$ and normalised $\dot{D}$ along the interface between the blocks within the middle

part in Fig. 3a

$\dot{W}^{\mathrm{rot}}$, $\bar{\dot{W}}^{\mathrm{rot}}$ $\dot{W}$ and normalised $\dot{W}$ of the rotational part in Fig. 3b

$\dot{D}^{\mathrm{rot}}$, $\bar{\dot{D}}^{\mathrm{rot}}$ $\dot{D}$ and normalised $\dot{D}$ along the wetting front beneath the rotational parts in Fig. 3b

$\dot{W}_{OABMG}$, $\bar{\dot{W}}_{OABMG}$ $\dot{W}$ and normalised $\dot{W}$ of the virtual mass (grey shaded area) in Fig. 3b

$\dot{W}_{OADG}$, $\bar{\dot{W}}_{OADG}$ $\dot{W}$ and normalised $\dot{W}$ of the total mass (including the grey and yellow shaded areas) in Fig. 3b

$f_{\gamma}^{\mathrm{mid}}$, $f_{\gamma}^{\mathrm{rot1}}$, $f_{\gamma}^{\mathrm{rot2}}$, $f_{\gamma}^{\mathrm{rot3}}$, $f_{c'}^{\mathrm{mid1}}$, $f_{c'}^{\mathrm{mid2}}$, $f_{c'}^{\mathrm{rot}}$ energy coefficients with subscripts γ and c' denoting gravity and cohesion terms and superscripts ‘mid’ and ‘rot’ being middle and rotational parts of the sliding mass

σ_z', τ_{zx} effective normal stress and shear stress at a point behind the wetting front

σ_m', $\sigma_m'^{f_+}$, $\sigma_m'^{f_-}$ mean stress in the Mohr’s circles shown in Fig. 6a where superscript ‘f_+’ and ‘f_-’ represent the active and passive failure state

$\sigma_x'^{f_+}$, $\sigma_x'^{f_-}$ slope-parallel stresses at active and passive failure states, respectively

$\sigma_x'^{\mathrm{f}}$ slope-parallel stress at the failure state

P, P_g slope-parallel and initial slope-parallel forces, respectively

P_a, P_p slope parallel force at active and passive failure states, respectively

References

Baum, R. L., J. W. Godt, & W. Z. Savage (2010), Estimating the timing and location of shallow rainfall-induced landslides using a model for transient, unsaturated infiltration, J. Geophys. Res., 115, F03013. https://doi:10.1029/2009JF001321

Borga, M., Dalla Fontana, G., Gregoretti, C., & Marchi, L. (2002). Assessment of shallow landsliding by using a physically based model of hillslope stability. Hydrol. Processes, 16(14), 2833–2851. https://doi.org/10.1002/hyp.1074

Bianchi, D., Gallipoli, D., Bovolenta, R., & Leoni, M. (2022). Analysis of unsaturated seepage in infinite slopes by means of horizontal ground infiltration models. Géotechnique, 1-9. https://doi.org/10.1680/jgeot.22.00042

Burroughs, E. R. J. (1985), Landslide hazard rating for portions of the Oregan Coast range paper presented at Symposium on effects of forest land use on erosion and slope stability, Univ. of Hawaii, Honolulu.

Casadei, M., Dietrich, W. E., & Miller, N. L. (2003). Testing a model for predicting the timing and location of shallow landslide initiation in soil-mantled landscapes. Earth. Surf. Process. Landf., 28(9), 925–950. https://doi.org/10.1002/esp.470

Cerdà, A., & García-Fayos, P. (1997). The influence of slope angle on sediment, water and seed losses on badland landscapes. Geomorphology, 18(2), 77–90. https://doi.org/10.1016/S0169-555X(96)00019-0

Chen, W. F. (1975). Limit analysis and soil plasticity. Amsterdam, Netherlands: Elsevier Science.

Chen, L., & Young, M. H. (2006). Green-Ampt infiltration model for sloping surfaces. Water Resour. Res., 42(7). https://doi.org/10.1029/2005WR004468

Chu-Agor, M. L., Fox, G. A., Cancienne, R. M., & Wilson, G. V. (2008). Seepage caused tension failures and erosion undercutting of hillslopes. J. Hydro., 359(3-4), 247–259. https://doi.org/10.1016/j.jhydrol.2008.07.005

Cislaghi, A., Cohen, D., Gasser, E., Bischetti, G. B., & Schwarz, M. (2019). Field measurements of passive earth forces in steep, shallow, landslide-prone areas. J. Geophys. Res.: Earth Surf., 124(3), 838–866. https://doi.org/10.1029/2017JF004557

Coe, J. A. (2020). Bellwether sites for evaluating changes in landslide frequency and magnitude in cryospheric mountainous terrain: a call for systematic, long-term observations to decipher the impact of climate change. Landslides, 17(11), 2483–2501. https://doi.org/10.1007/s10346-020-01462-y

Collins, B. D., & Znidarcic, D. (2004). Stability analyses of rainfall induced landslides. J. Geotech. Geoenviron. Eng., 130(4), 362–372. https://doi.org/10.1061/(ASCE)1090-0241(2004)130:4(362)

Conte, E., Pugliese, L., & Troncone, A. (2022). A Simple Method for Predicting Rainfall-Induced Shallow Landslides. J. Geotech. Geoenviron. Eng., 148(10), 04022079. https://orcid.org/0000-0002-2008-0381

Conte, E., & Troncone, A. (2012). Simplified approach for the analysis of rainfall-induced shallow landslides. J. Geotech. Geoenviron. Eng., 138(3), 398–406. https://doi.org/10.1061/(ASCE)GT.1943-5606.0000577

Correa, O., García, F., Bernal, G., Cardona, O. D., & Rodriguez, C. (2020). Early warning system for rainfall-triggered landslides based on real-time probabilistic hazard assessment. Nat. Hazards., 100, 345-361. https://doi.org/10.1007/s11069-019-03815-w

Dai, F. C., Lee, C. F., & Wang, S. J. (2003). Characterisation of rainfall-induced landslides. Int. J. Remote Sens., 24(23), 4817–4834. https://doi.org/10.1080/01431160131000082424

Fredlund, D. G., & Rahardjo, H. (1993). Soil Mechanics for Unsaturated Soils. Wiley, New York, NY, USA.

Gabet, E. J., & T. Dunne (2002). Landslides on coastal sage-scrub and grassland hillslopes in a severe El Nino winter: The effects of vegetation conversion on sediment delivery, Geol. Soc. Am. Bull., 114(8), 983–990. https://doi.org/10.1130/0016-7606(2002)114%3C0983:LOCSSA%3E2.0.CO;2

Gariano, S. L. & Guzzetti, F. (2016). Landslides in a changing climate. Earth-Sci. Rev., 162, 227–252. https://doi.org/10.1016/j.earscirev.2016.08.011, 2016

Green, W. H., & G. A. Ampt. (1911). Studies on soil physics, J. Agric. Sci., 4(1), 1–24. https://doi.org/10.1017/S0021859600001441

Griffiths, D. V., Huang, J., & Dewolfe, G. F. (2011). Numerical and analytical observations on long and infinite slopes. Int. J. Numer. Anal. Methods Geomech., 35(5), 569–585. https://doi.org/10.1002/nag.909

Gutierrez-Martin, A. (2020). A GIS-physically-based emergency methodology for predicting rainfall-induced shallow landslide zonation. Geomorphology, 359, 107121. https://doi.org/10.1016/j.geomorph.2020.107121

Handwerger, A. L., Fielding, E. J., Huang, M. H., Bennett, G. L., Liang, C., & Schulz, W. H. (2019). Widespread initiation, reactivation, and acceleration of landslides in the northern California Coast Ranges due to extreme rainfall. J. Geophys. Res.: Earth Surf., 124(7), 1782–1797. https://doi.org/10.1029/2019JF005035

Healy, R. W., & Cook, P. G. (2002). Using groundwater levels to estimate recharge. Hydrogeol J., 10, 91–109. https://doi.org/10.1007/s10040-001-0178-0

Huang, W., Loveridge, F., & Satyanaga, A. (2022). Translational upper bound limit analysis of shallow landslides accounting for pore pressure effects. Comput. Geotech., 148, 104841. https://doi.org/10.1016/j.compgeo.2022.104841

Iverson, R. M. (2000), Landslide triggering by rain infiltration, Water Resour. Res., 36(7), 1897–1910. https://doi:10.1029/2000WR900090

Jaky J. 1944. The coefficient of earth pressure at rest. Journal of the Society of Hungarian Architects and Engineers, Budapest, Hungary, 355-358 (in Hungarian).

Jana, R. B., & Mohanty, B. P. (2012). On topographic controls of soil hydraulic parameter scaling at hillslope scales. Water Resour. Res., 48(2). https://doi.org/10.1029/2011WR011204

Jotisankasa, A., & Mairaing, W. (2010). Suction-monitored direct shear testing of residual soils from landslide-prone areas. J. Geotech. Geoenviron. Eng., 136(3), 533–537. https://doi.org/10.1061/(ASCE)GT.1943-5606.00002

Kjekstad, O. & Highland, L. (2009). Economic and social impacts of landslides. In Landslides–disaster risk reduction. 573–587. Springer, Berlin, Heidelberg.

Krabbenhoft, K., 2019. OptumG2: Theory, Optum Computational Engineering. Available at www.optumce.com.

Lee, L. M., Gofar, N., & Rahardjo, H. (2009). A simple model for preliminary evaluation of rainfall-induced slope instability. Eng. Geol., 108(3-4), 272–285. https://doi.org/10.1016/j.enggeo.2009.06.011

Lehmann, P., & Or, D. (2012). Hydromechanical triggering of landslides: From progressive local failures to mass release. Water Resour. Res., 48(3). https://doi.org/10.1029/2011WR010947

Mein, R. G., & Larson, C. L. (1973). Modeling infiltration during a steady rain. Water Resour. Res., 9(2), 384–394. https://doi.org/10.1029/WR009i002p00384

Milledge, D. G., Bellugi, D., McKean, J. A., Densmore, A. L., & Dietrich, W. E. (2014). A multidimensional stability model for predicting shallow landslide size and shape across landscapes. J. Geophys. Res.: Earth Surf., 119(11), 2481–2504. https://doi.org/10.1002/2014JF003135

Milledge, D. G., Griffiths, D. V., Lane, S. N., & Warburton, J. (2012). Limits on the validity of infinite length assumptions for modelling shallow landslides. Earth. Surf. Process. Landf., 37(11), 1158–1166. https://doi.org/10.1002/esp.3235

Muntohar, A. S., & Liao, H. J. (2010). Rainfall infiltration: infinite slope model for landslides triggering by rainstorm. Nat. hazards., 54, 967–984. https://doi.org/10.1007/s11069-010-9518-5

Ng, C. W. W., Zhan, L. T., Bao, C. G., Fredlund, D. G., & Gong, B. W. (2003). Performance of an unsaturated expansive soil slope subjected to artificial rainfall infiltration. Géotechnique, 53(2), 143–157. https://doi.org/10.1680/geot.2003.53.2.143

Osman, A. S. (2019). Upper bound solutions for the shape factors of smooth rectangular footings on frictional materials. Comput. Geotech., 115, 103177. https://doi.org/10.1016/j.compgeo.2019.103177

Petley, David. (2012). Global patterns of loss of life from landslides. Geology, 40(10), 927–930. https://doi.org/10.1130/G33217.1

Puzrin, A.M. (2016). Simple criteria for ploughing and runout in post-failure evolution of submarine landslides. Can. Geotech. J., 53(8), 1305–1314. https://doi.org/10.1139/cgj-2015-0582

Puzrin, A. M., Gray, T. E., & Hill, A. J. (2015). Significance of the actual nonlinear slope geometry for catastrophic failure in submarine landslides. Proceedings of the Royal Society A: Mathematical, Physical and Engineering Sciences, 471(2175), 20140772. https://doi.org/10.1098/rspa.2014.0772

Rahardjo, H., Lim, T. T., Chang, M. F., & Fredlund, D. G. (1995). Shear-strength characteristics of a residual soil. Can. Geotech. J., 32(1), 60–77. https://doi.org/10.1139/t95-005

Rahardjo, H., Lee, T. T., Leong, E. C., & Rezaur, R. B. (2005). Response of a residual soil slope to rainfall. Can. Geotech. J., 42(2), 340–351. https://doi.org/10.1139/t04-101

Ran, Q., Hong, Y., Li, W., & Gao, J. (2018). A modelling study of rainfall-induced shallow landslide mechanisms under different rainfall characteristics. J. Hydrol., 563, 790–801.

https://doi.org/10.1016/j.jhydrol.2018.06.040

Silliman, S. E., Berkowitz, B., Simunek, J., & Van Genuchten, M. T. (2002). Fluid flow and solute migration within the capillary fringe. Groundwater, 40(1), 76–84. https://doi.org/10.1111/j.1745-6584.2002.tb02493.x

Tan, B. K., & Ting, W. H. (2008). Some Case Studies on Debris Flow in Peninsular Malaysia. In Geotechnical Engineering for Disaster Mitigation and Rehabilitation: Proceedings of the 2nd International Conference GEDMAR08, Nanjing, China 30 May–2 June, 2008 (pp. 231-235). Springer Berlin Heidelberg.

Tran, T. V., Alvioli, M., Lee, G., & An, H. U. (2018). Three-dimensional, time-dependent modeling of rainfall-induced landslides over a digital landscape: a case study. Landslides, 15, 1071–1084. https://doi.org/10.1007/s10346-017-0931-7

Vo, T., & Russell, A. R. (2017). Stability charts for curvilinear slopes in unsaturated soils. Soils Found., 57(4), 543–556. https://doi.org/10.1016/j.sandf.2017.06.005

von Ruette, J., Lehmann, P., & Or, D. (2013). Rainfall-triggered shallow landslides at catchment scale: Threshold mechanics-based modeling for abruptness and localisation. Water Resour. Res., 49(10), 6266–6285. https://doi.org/10.1002/wrcr.20418

Wang, H., Sun, P., Zhang, S., Ren, J., Wang, T., & Xin, P. (2022). Evolutionary and dynamic processes of the Zhongzhai landslide reactivated on October 5, 2021, in Niangniangba, Gansu Province, China. Landslides, 19(12), 2983–2996. https://doi.org/10.1007/s10346-022-01966-9

Yates, K., & Russell, A. R. (2022). The unsaturated characteristics of natural loess in slopes, New Zealand. Géotechnique, 1–14. https://doi.org/10.1680/jgeot.21.00042

Zhan, T. L., Jia, G. W., Chen, Y. M., Fredlund, D. G., & Li, H. (2013). An analytical solution for rainfall infiltration into an unsaturated infinite slope and its application to slope stability

analysis. Int. J. Numer. Anal. Methods Geomech., 37(12), 1737–1760. https://doi.org/10.1002/nag.2106

Zhang, L. L., Zhang, J., Zhang, L. M., & Tang, W. H. (2011). Stability analysis of rainfall-induced slope failure: a review. Proceedings of the Institution of Civil Engineers-Geotechnical Engineering, 164(5), 299–316. https://doi.org/10.1680/geng.2011.164.5.299

Zhang, L., Li, J., Li, X., Zhang, J., & Zhu, H. (2018). Rainfall-induced soil slope failure: stability analysis and probabilistic assessment. CRC Press.

Zhang, W., Wang, D., Randolph, M. F., & Puzrin, A. M. (2017). From progressive to catastrophic failure in submarine landslides with curvilinear slope geometries. Géotechnique, 67(12), 1104–1119. https://doi.org/10.1680/jgeot.16.P.249

Zhang, W., Klein, B., Randolph, M. F., & Puzrin, A. M. (2021). Upslope failure mechanisms and criteria in submarine landslides: Shear band propagation, slab failure and retrogression. J. Geophys. Res.: Solid Earth, 126(9), e2021JB022041. https://doi.org/10.1029/2021JB022041

Zhu, J. H. & Anderson, S. A. (1998). Determination of shear strength of Hawaiian residual soil subjected to rainfall-induced landslides. Géotechnique, 48(1), 73–82. https://doi.org/10.1680/geot.1998.48.1.73

Accepted manuscript doi:
10.1680/jgeot.23.00263

Tables

Table 1 Controlling parameters related to h_w, Z_0 and r_0 for the translational failure mechanism shown in Fig. 3

Parameters	Expressions
Coordinate θ at point *D*, θ_0 (rad)	$\theta_0 = \pi/2 - \text{atan}[(H - Z_0)\tan\beta_c/H] + \varphi'$
Slope angle β at point *D*, β_0 (rad)	$\beta_0 = \text{atan}[(H - Z_0)\tan\beta_c/H]$
Coordinate X at point *D*, X_0 (m)	$X_0 = -H\ln(1 - Z_0/H)/\tan\beta_c$
Coordinate r at point *A*, r_A (m)	$r_A = r_0\exp[(\theta_A - \theta_0)\tan\varphi']$
Coordinate r at point *G*, r_G (m)	$r_G = r_0\exp[(\theta_G - \theta_0)\tan\varphi']$
Coordinate θ at point *A*, θ_A (rad) Coordinate θ at point *G*, θ_G (rad)	$r_0\sin\theta_0 - r_A\sin\theta_A + Z_0 - h_w = \bar{A}H$ $r_0\sin\theta_0 - r_G\sin\theta_G - Z_0 - h_w = -\bar{B}H$ (Constraint equations)
Coefficient f_γ^{mid}	$f_\gamma^{\text{mid}} = \frac{r_0}{H}\begin{bmatrix}2\cos^2\varphi'\ln(\bar{C}/\bar{D})/[\sin(\varphi' - \beta_0)\tan\beta_c] \\ -\sin 2\varphi'\,[\ln(\bar{C}/\bar{D}) + \ln(H/(H - Z_0))]/[\cos(\varphi' - \beta_0)\tan\beta_c]\end{bmatrix}$

Accepted manuscript doi:
10.1680/jgeot.23.00263

	f_γ^{rot1}
Coefficient f_γ^{rot1}	$= \dfrac{(3\tan\varphi'\cos\theta_G + \sin\theta_G)r_G^3 - (3\tan\varphi'\cos\theta_A + \sin\theta_A)r_A^3}{3(1+9\tan^2\varphi')H^3}$
	f_γ^{rot2}
Coefficient f_γ^{rot2}	$= \dfrac{1}{6H^3}\begin{bmatrix}2((r_G\cos\theta_G)^3\tan\theta_G - (r_A\cos\theta_A)^3\tan\theta_A) \\ +3(r_0\sin\theta_0 + Z_0 - H)(r_A\cos\theta_A)^2 - 3(r_0\sin\theta_0 - Z_0 + H) \\ +6\bar{E}\,H^2(H-Z_0)/\tan^2\beta_c + 6\bar{F}\,H(H-Z_0)/\tan\beta_c\end{bmatrix}$
Coefficient f_γ^{rot3}	$f_\gamma^{\mathrm{rot3}} = [(r_G\cos\theta_G)^2 - (r_A\cos\theta_A)^2]/2H^2$
	$f_{c'}^{\mathrm{mid1}}$
Coefficient $f_{c'}^{\mathrm{mid1}}$	$= \dfrac{2r_0c'\cos^2\varphi'}{\gamma H^2}\left[\begin{matrix}\ln(\bar{C}/\bar{D})/[\cos(\varphi'-\beta_0)\sin^2(\varphi'-\beta_0)\tan\beta_c] \\ +\dfrac{\ln(H/(H-Z_0))}{\cos(\varphi'-\beta_0)\tan\beta_c} - \dfrac{Z_0}{H\sin(\varphi'-\beta_0)}\end{matrix}\right]$
Coefficient $f_{c'}^{\mathrm{mid2}}$	$f_{c'}^{\mathrm{mid2}} = \dfrac{2r_0c'\cos\varphi'\cos(\varphi'-\beta_0)\sin(\beta_c-\beta_0)}{\gamma H^2\cos(\beta_c-\beta_0+\varphi')}$
Coefficient $f_{c'}^{\mathrm{rot}}$	$f_{c'}^{\mathrm{rot}} = \dfrac{c'r_0^2}{2\gamma H^3\tan\varphi'}[\exp(2(\theta_G-\theta_0)\tan\varphi') - \exp(2(\theta_A-\theta_0)\tan\varphi')]$

*Coefficient $\bar{A}$, $\bar{B}$, $\bar{C}$, $\bar{D}$, $\bar{E}$, and $\bar{F}$ in above expressions, respectively, are (see supplementary materials for more details)

$\bar{A} = 1 - \exp[(r_0\cos\theta_0 - r_A\cos\theta_A)\tan\beta_c/H + \ln(1-Z_0/H)]$, $\bar{C} = H\cos(\varphi'-\beta_0) - (H-Z_0)\sin(\varphi'-\beta_0)\tan\beta_c$,

$\bar{B} = 1 - \exp[(r_G\cos\theta_G - r_0\cos\theta_0)\tan\beta_c/H + \ln(1-Z_0/H)]$, $\bar{D} = H\cos(\varphi'-\beta_0) - H\sin(\varphi'-\beta_0)\tan\beta_c$,

$\bar{E} = [1-\exp(r_G\cos\theta_G\tan\beta_c/H)]\exp(-r_0\cos\theta_0\tan\beta_c/H) + [1-\exp(-r_A\cos\theta_A\tan\beta_c/H)]\exp(r_0\cos\theta_0\tan\beta_c/H)$,

$\bar{F} = r_G\cos\theta_G\exp[(r_G\cos\theta_G - r_0\cos\theta_0)\tan\beta_c/H] - r_A\cos\theta_A\exp[(r_0\cos\theta_0 - r_A\cos\theta_A)\tan\beta_c/H]$.

Accepted manuscript doi:
10.1680/jgeot.23.00263

Table 2 Comparisons of the critical wetting front depths and slide lengths from the proposed methods and the finite element limit analysis for both upper- and lower-bound analyses. LBLA – lower-bound limit analysis; UBLA – upper-bound limit analysis; AF – active failure; PF – passive failure

Cases	β_c (°)	H (m)	Critical wetting front depth h_w (m)					Slide length L (m)			
			Finite element LBLA	Finite element UBLA	Proposed LBLA		Proposed UBLA	Finite element LBLA	Finite element UBLA	Proposed LBLA	Proposed UBLA
					AF	PF					
Case 1	42	40	4.05	4.15	2.73	3.32	4.17	32.41	33.50	18.05	35.36
Case 2	45	35	3.24	3.33	2.43	2.89	3.33	26.75	26.83	17.37	28.52
Case 3	50	25	2.74	2.82	2.13	2.51	2.88	19.52	19.59	14.46	21.06

Accepted manuscript doi:
10.1680/jgeot.23.00263

Table 3 The basic properties of the sandy silt used in analysis

Parameter	Value	Unit
Saturated volumetric water content, θ_s	0.44	
Specific gravity, G_s	2.63	
Unit weight of the water, γ_w	10	kN/m^3
Friction angle related to matric suction, φ^b	18	°
Effective cohesion, c'	7.6	kPa
Effective friction angle, φ'	32.1	°
At-rest earth pressure coefficient, K_0	0.469	

Accepted manuscript doi:
10.1680/jgeot.23.00263

Figure captions

Fig. 1 (a) Possible water content and suction profiles in residual soils after drainage (modified after Healy & Cook 2002); (b) Transient suction profiles during rainwater recharge (modified after Rahardjo et al. 1995)

Fig. 2 Progressive failure process of a shallow landslide induced by rainfall

Fig. 3 The proposed failure mechanism in upper-bound analysis. (a) overall failure extension; (b) rotational failure part; (c) hodograph for the failure mechanism in the middle part

Fig. 4 The flowchart for the calculation of the critical wetting front and failure positions using the proposed approximate upper- and lower-bound solutions

Fig. 5 The stress state behind the wetting front and the development of slope-parallel force

Fig. 6 Stress states of a material point in Mohr's circles for active and passive failure (a) where $\beta \leq \varphi'$ and (b) $\beta > \varphi'$

Fig. 7 Failure mechanisms for Case 2, where the displacement contour is obtained by finite element UBLA with Optum G2: (a) a global rotational failure mechanism before rainfall at the initial state; (b) a shallow translational failure mechanism at the critical state obtained by finite element UBLA, proposed UBLA, and proposed LBLA

Fig. 8 (a) Simplified planar slope models with different slope angles for a curvilinear slope; (b) Comparisons of the critical wetting depths obtained by proposed UBLA, LBLA, ISM, and SPSM (Huang et al. 2022)

Fig. 9 The obtained critical wetting front depth and slide length with the proposed UBLA and LBLA against (a) the cohesion of the soil, (b) at-rest earth pressure coefficient, and (c) the maximum slope angle at centre

Fig. 10 (a) Location of the study area in Peninsula, Malaysia; (b) matric suction profiles along the soil depth in a sandy silt slope under different rainfall patterns based on a ten-year return period in Peninsula, Malaysia (Adapted from Lee et al. 2009); (c) the obtained critical wetting front depths against various centre slope angles

Accepted manuscript doi:
10.1680/jgeot.23.00263

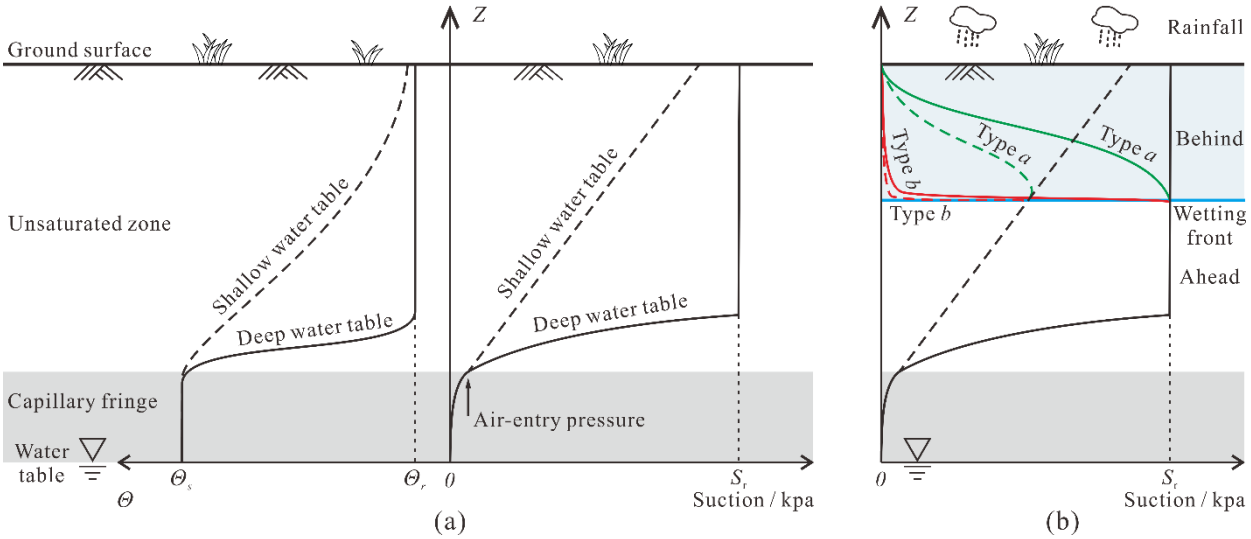

Figure 1

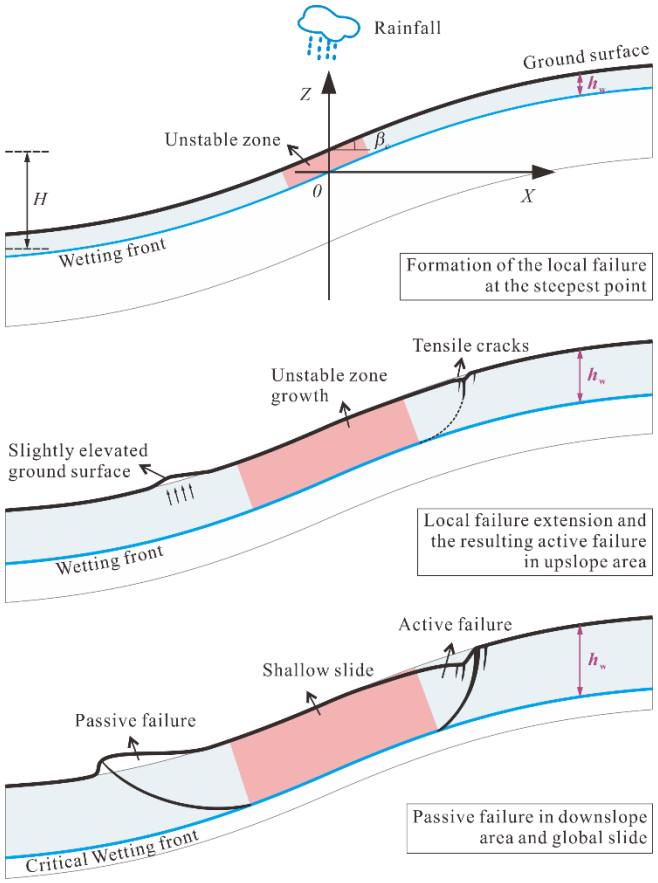

Figure 2

Accepted manuscript doi:
10.1680/jgeot.23.00263

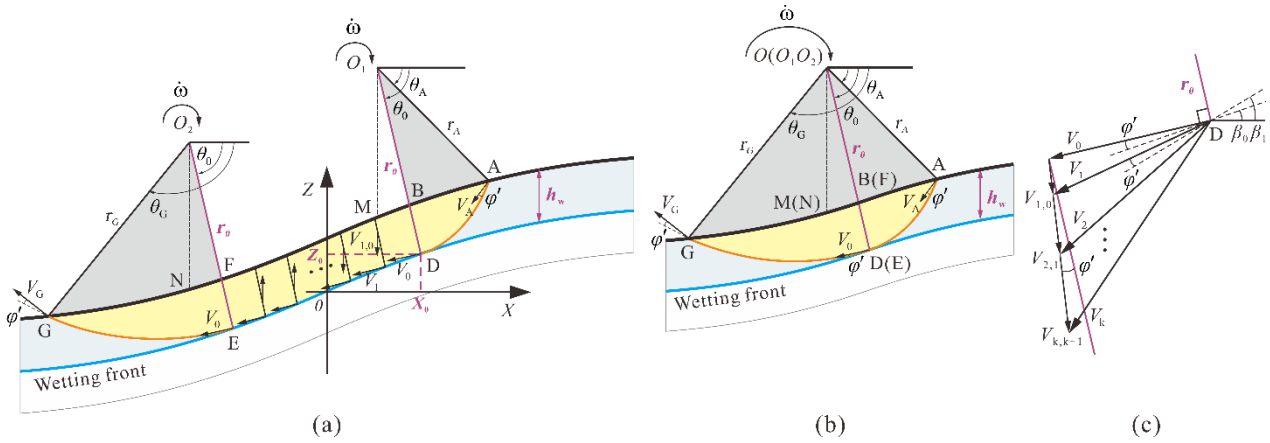

Figure 3

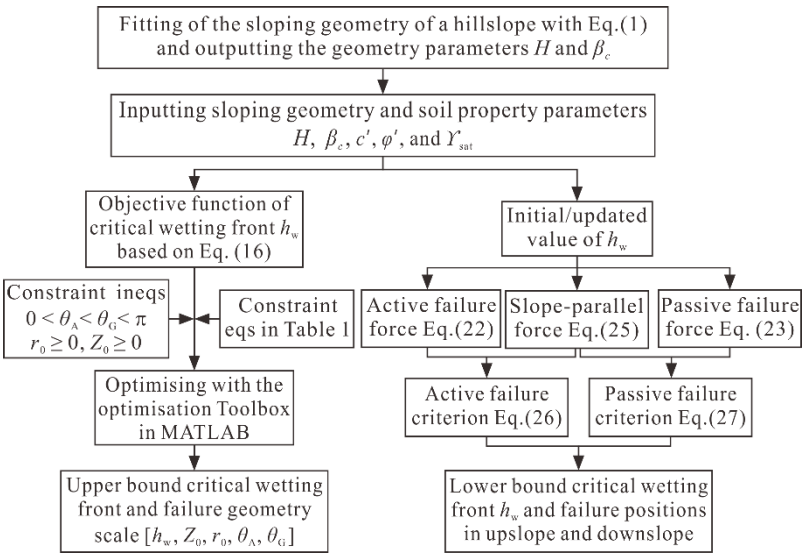

Figure 4

Accepted manuscript doi:
10.1680/jgeot.23.00263

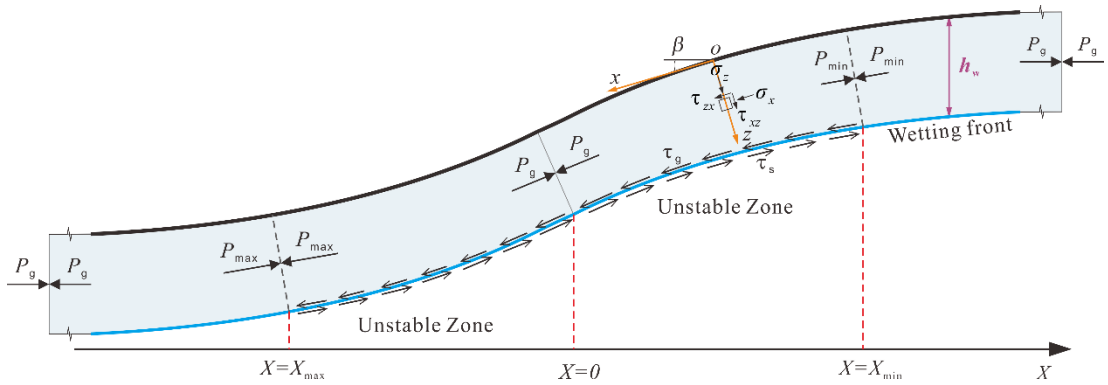

Figure 5

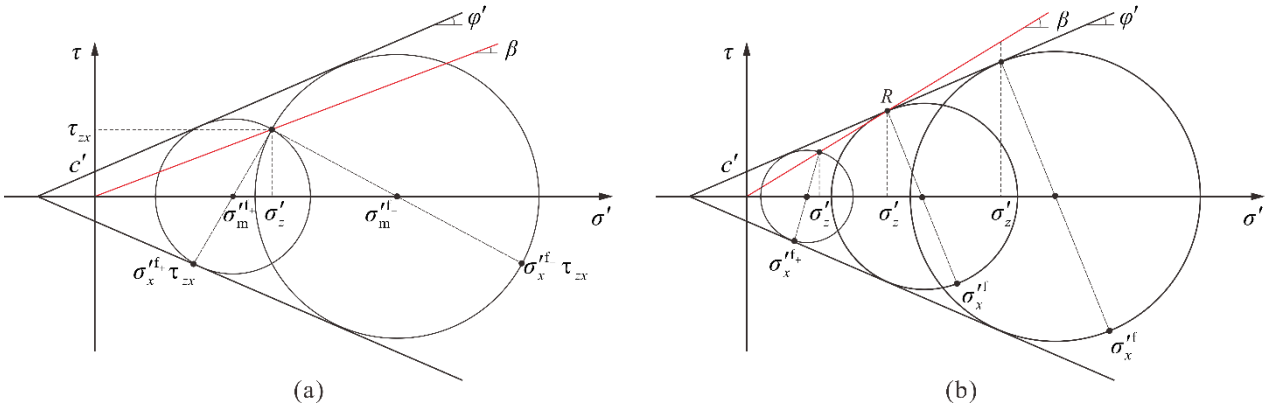

Figure 6

Accepted manuscript doi:
10.1680/jgeot.23.00263

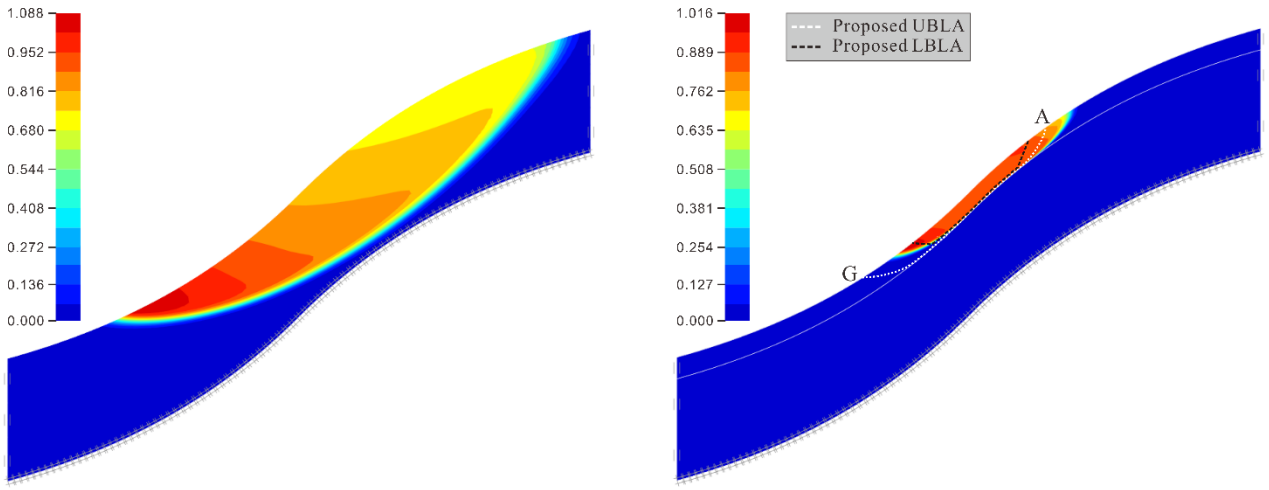

(a) Initial state (FOS=1.127) (b) Critical state (FOS=1)

Figure 7

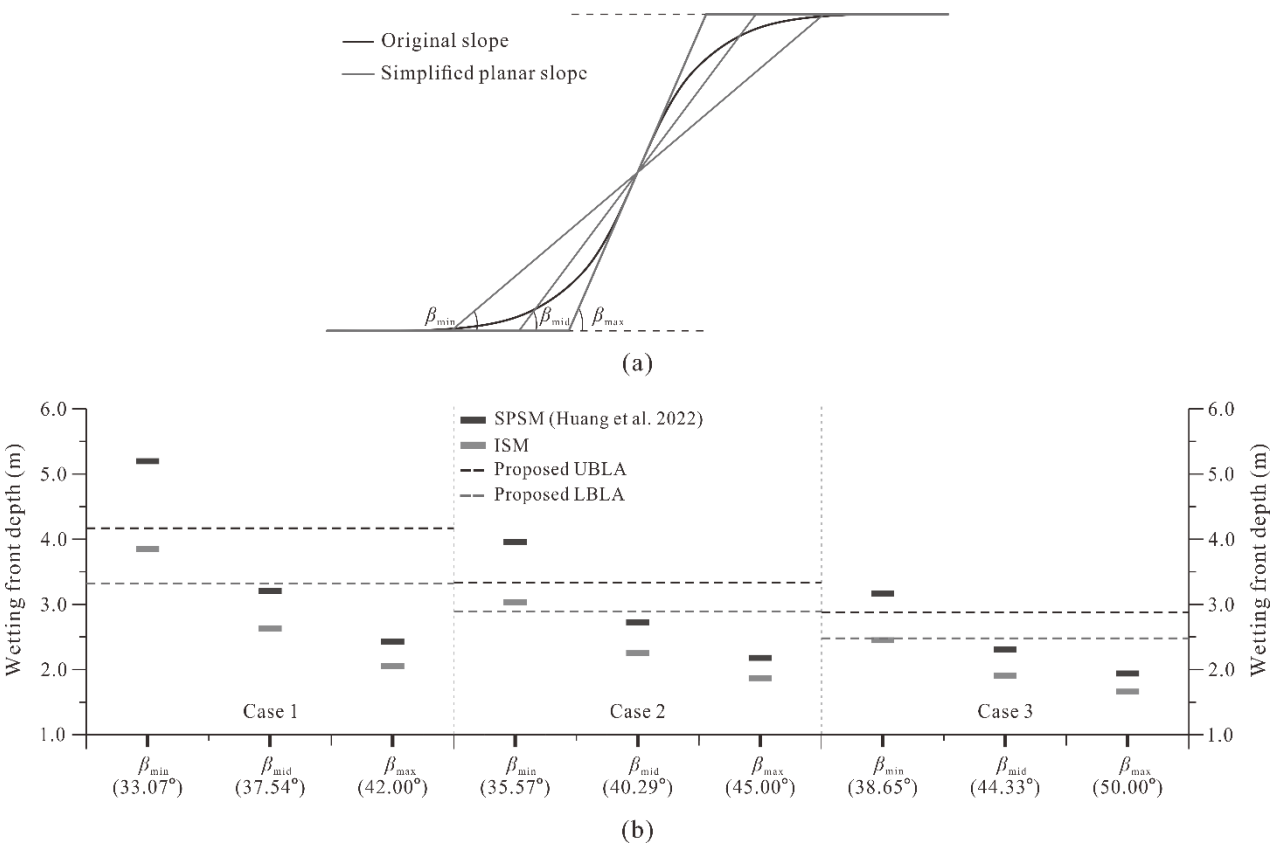

Figure 8

Accepted manuscript doi:
10.1680/jgeot.23.00263

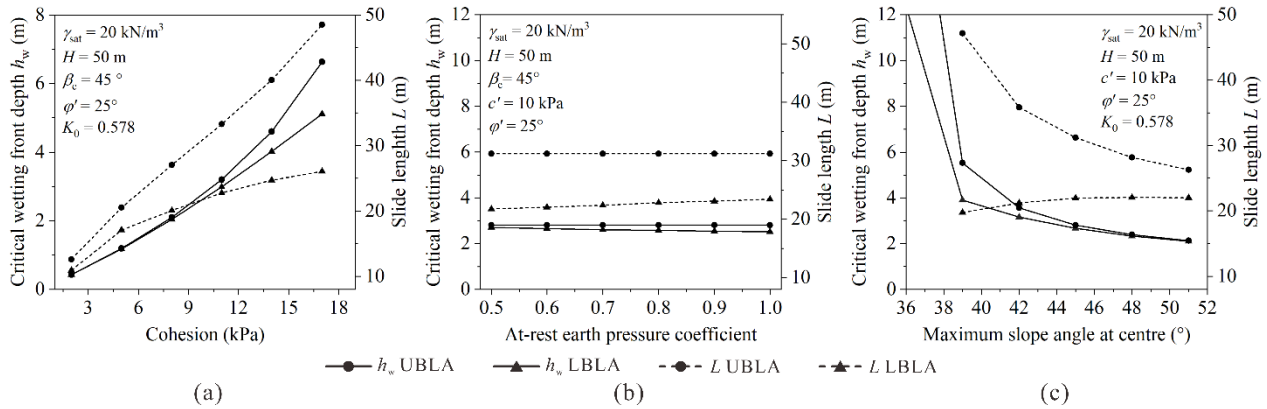

Figure 9

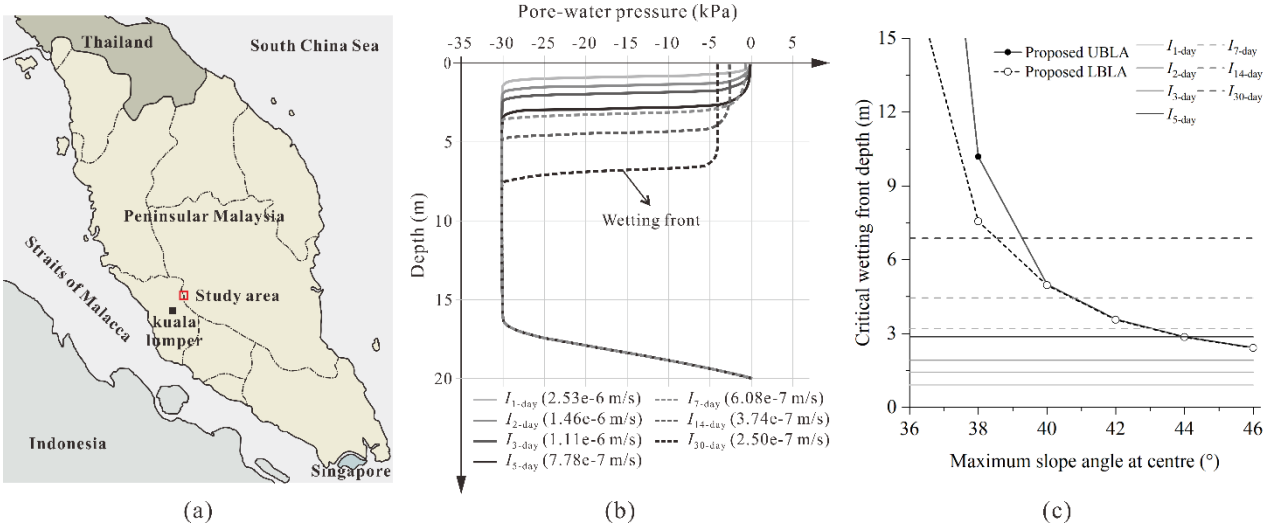

Figure 10